WILDFIRES

Smoke-weather interaction affects extreme wildfires in diverse coastal regions

Xin Huang[1,2]†*, Ke Ding[1,2]†, Jingyi Liu[1], Zilin Wang[1], Rong Tang[1], Lian Xue[1], Haikun Wang[1,2], Qiang Zhang[3], Zhe-Min Tan[1], Congbin Fu[1], Steven J. Davis[3,4], Meinrat O. Andreae[5,6,7], Aijun Ding[1,2]*

Extreme wildfires threaten human lives, air quality, and ecosystems. Meteorology plays a vital role in wildfire behaviors, and the links between wildfires and climate have been widely studied. However, it is not fully clear how fire-weather feedback affects short-term wildfire variability, which undermines our ability to mitigate fire disasters. Here, we show the primacy of synoptic-scale feedback in driving extreme fires in Mediterranean and monsoon climate regimes in the West Coast of the United States and Southeastern Asia. We found that radiative effects of smoke aerosols can modify near-surface wind, air dryness, and rainfall and thus worsen air pollution by enhancing fire emissions and weakening dispersion. The intricate interactions among wildfires, smoke, and weather form a positive feedback loop that substantially increases air pollution exposure.

In recent decades, wildfires have increasingly threatened lives and infrastructure, degraded air quality, and damaged ecosystem services (*1*–*3*). Globally, wildfires account for ~25% of the world's forest loss and ~8% of premature deaths from poor air quality (*4*, *5*). The intensity of wildfires is extremely heterogeneous and largely determined by meteorology on a range of temporal scales (*6*, *7*). Meteorology affects vegetation productivity (fuel availability), determines the length of fire seasons (fuel flammability), and influences the spread of the fires (fire behavior), yet prior studies of the fire-meteorology relationship have mostly focused on long-term climate scale (*8*, *9*) rather than short-term weather processes. Anomalous synoptic weather conditions at time scales of ~1 to 2 weeks, such as exceptionally strong winds that drive rapid fire spread (*10*) and intense hydrological droughts that make vegetation extremely combustible (*11*), have important impacts on the behavior of extreme wildfires (*12*, *13*). The recent increase in catastrophic wildfires globally (*6*, *14*) calls into question our understanding of the drivers of extreme wildfire events, as well as our capacity to manage the most severe fires, especially in regions with dense populations.

In general, wildfires exhibit great variability on temporal scales, ranging from days to years, but extreme wildfires (i.e., >90th percentile of daily burned area in one specific fire-prone region) are tightly linked to synoptic fluctuations (*15*, *16*). To quantitatively understand the temporal scales of wildfires, we applied empirical mode decomposition and Fourier transform to daily burned area in major wildfire regions during 2002–2021 (see the materials and methods). Figure 1 shows that synoptic-scale (<20 days) variation of wildfires is evident in most fire-prone areas across the globe. Among them, the US West Coast and Southeastern Asia are characterized by the most pronounced fluctuations down to 1 to 2 weeks, corresponding to the time period of extreme fires that have repeatedly ravaged both regions (*17*). Given the dense populations in these regions, the impacts of these fires on air quality and the associated human health exposure are enormous (*18*, *19*).

During extreme fire events, weather conditions show distinct patterns in both regions with respect to key meteorological drivers such as relative humidity, wind speed, and precipitation (Fig. 1). In the US West Coast, which has a Mediterranean climate, extreme fires usually begin when near-surface humidity is very low and wind speeds are at their highest. During these periods, dry air rapidly lowers vegetation moisture while strong winds accelerate the rate of fire spread, and the compounding effect of these two drivers gives rise to large and severe fires (*10*). By contrast, the variability of rainfall in the monsoon climate of Southeastern Asia largely determines the magnitude of the fire activity, with rainfall deficits making fuels flammable and drying peatlands (*20*).

Meteorological parameters such as humidity, wind speed, and precipitation are key factors modulating extreme wildfires (*14*, *21*), whereas radiatively active aerosols such as black carbon (BC) in fire smoke may create feedback by substantially altering meteorology (*22*–*24*). However, relatively little attention has been paid to the complex interactions among smoke aerosols, weather, and wildfire behaviors on a synoptic scale. We used a coupled meteorology-chemistry model together with multiple satellite and ground-based observational datasets to investigate the role of fire-weather feedback in the spread and impacts of extreme wildfires for the two regions with the largest synoptic-scale variability in wildfires.

The US West Coast is suffering from increasingly destructive wildfires, with records broken every few years (*10*, *25*), and the wildfire-induced severe haze pollution has long been a top air-quality concern there (*26*). In September 2020, a series of wildfires in Oregon and California burned 1.2 million acres (defined as a "gigafire" for an area >1 million acres; fig. S1). Fire smoke stretched from the Pacific Ocean over most of Oregon, California, and even Canada (Fig. 2), and hazardous haze pollution engulfed valley cities (*10*). During this gigafire, the observed near-surface specific humidity and wind speed reached unprecedented levels of 3.3 g/m^3 and 13.1 m/s, respectively, in the western Oregon Cascades. Correspondingly, there were strong anomalies compared with the climatic mean in the large fire potential (LFP) index (see the supplementary materials).

To explore the interaction mechanism among smoke aerosols, meteorology, and this gigafire, we conducted meteorology-chemistry–coupled simulations using the WRF-Chem model (see the supplementary materials). Smoke aerosols modify meteorology through impacts on both radiation transfer and clouds. Given the cloudless skies over the US West Coast during the gigafire (fig. S2), we performed two parallel experiments, one with an aerosol-radiation interaction (EXP_ARI) and the other without (EXP_nARI), and validated the model with in situ and remote sensing measurements (figs. S3 and S4). During the most severe haze pollution (10 to 13 September 2020), aerosol optical depth (AOD) sharply increased from ~0.2 to >2. Such a high aerosol loading substantially perturbed the radiation energy balance by trapping >100 W/m^2 (~32%) of incoming solar energy in the atmosphere and in turn altered thermal stratification (fig. S5).

The light absorption by aerosol tended to warm the smoke layer and cool the land surface over the US West Coast, thereby suppressing the development of the planetary boundary layer (PBL), a phenomenon known as the aerosol-PBL interaction (*27*). On 12 September 2020, the decrease in near-surface temperature was 6°C in Salem, Oregon, accompanied by a decline in daytime PBL height of >500 m (~63%). Further, our results show that the aerosol-PBL interaction increased near-surface fine particle concentrations ($PM_{2.5}$) by >100 μg/m^3 on the western slope of the Cascade Mountains

[1]School of Atmospheric Sciences, Nanjing University, Nanjing 210023, China. [2]Frontiers Science Center for Critical Earth Material Cycling, Nanjing University, Nanjing 210023, China. [3]Department of Earth System Science, Tsinghua University, Beijing 100084, China. [4]Department of Earth System Science, University of California, Irvine, CA 92697, USA. [5]Max Planck Institute for Chemistry, 55128 Mainz, Germany. [6]Scripps Institution of Oceanography, University of California, San Diego, La Jolla, CA 92093, USA. [7]Department of Geology and Geophysics, King Saud University, Riyadh 145111, Saudi Arabia.
*Corresponding author. Email: dingaj@nju.edu.cn (A.D.); xinhuang@nju.edu.cn (X.H.)
†These authors contributed equally to this work.

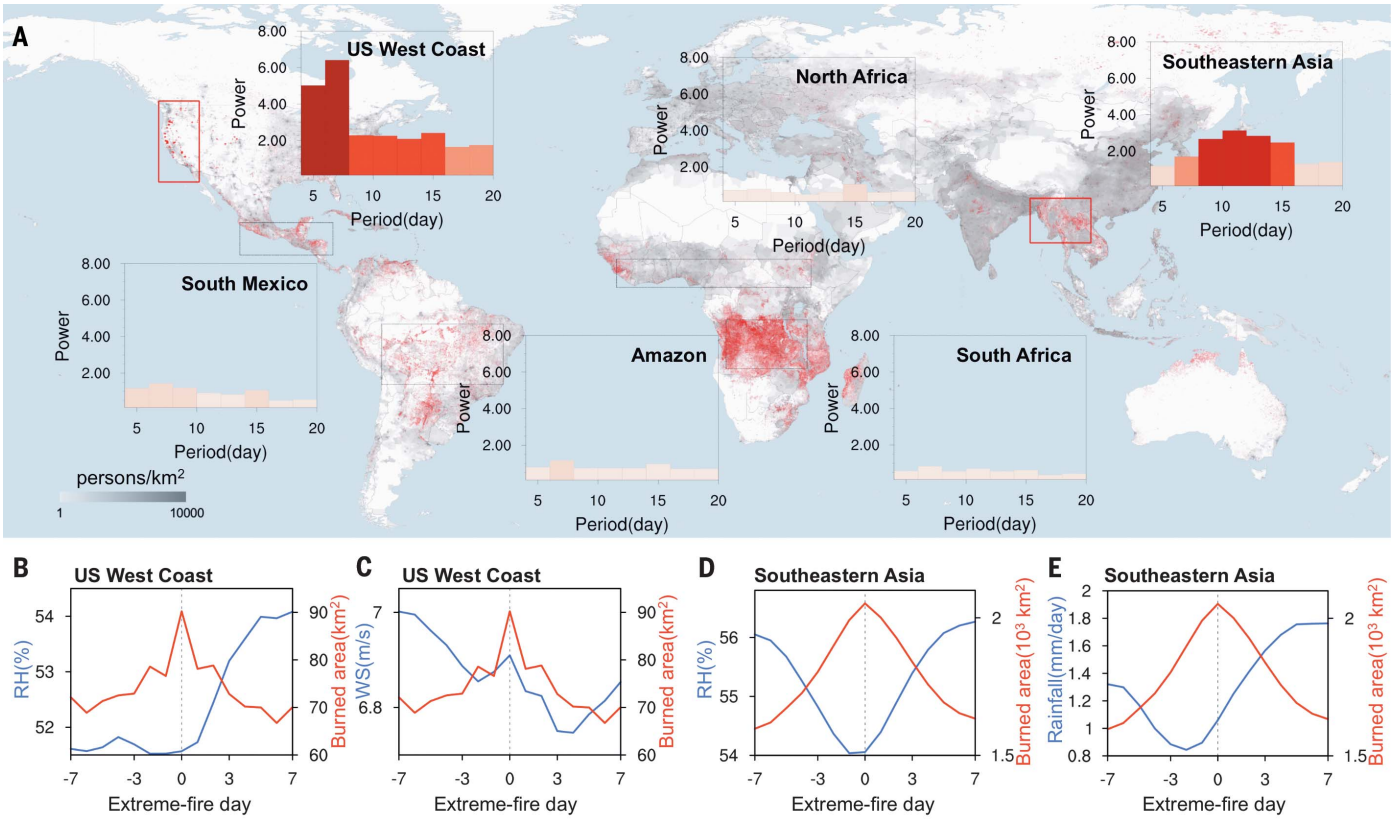

Fig. 1. Synoptic-scale variability of wildfires and meteorology during extreme fires in typical fire regions in the globe. (**A**) Global map of population density and power spectra of burned area variation at synoptic scale in main fire-prone regions based on empirical mode decomposition and Fourier transform (see the materials and methods). The Fourier power at different oscillation periods is color coded. Six typical wildfire regions are marked by rectangles. (**B** and **C**) Two-week evolution of 2-m relative humidity (RH) and 10-m wind speed (WS_{10}) derived from ERA5 reanalysis data around extreme fires (daily burned area >90th percentile) in the US West Coast during 2002–2021. The day with the largest fire area is indicated as a dashed line in the middle (day 0). (**D** and **E**) Two-week evolution of RH and rainfall rate around extreme fires in Southeastern Asia. The US West Coast and Southeastern Asia regions are outlined by red rectangles in (A).

during 10 to 13 September 2020 (Fig. 2D), due mainly to the smoke-stabilized PBL trapping pollution in a much shallower PBL.

The fire smoke also substantially modified vertical and horizontal winds because the reallocated radiative energy caused a katabatic and offshore wind anomaly. Specifically, land cooling led to a strong easterly wind anomaly of 3 to 4 m/s in near-surface wind, especially at the western slope of the Cascade Mountains. Furthermore, the aerosol-PBL interaction over the land area with high AOD prevented the onshore transport of water vapor from the Pacific Ocean. Thus, the near-surface air was dried out over the fire-prone areas, which is exactly the area with abnormally intense wildfires and severe pollution compared with the climatological average (fig. S6). Associated with the enhanced downslope wind, the windspeed was amplified (Fig. 2D). The specific humidity deficit and wind speed increase induced by the smoke aerosols correlated well with AOD (Fig. 2E). Such synchronous reinforcements in the two major meteorological drivers of extreme wildfires are tightly coupled. The Mediterranean climate and topography in the US West Coast shape a marked meridional humidity gradient in summer (fig. S6C), so the enhanced easterly winds would further dry out the air (*28*). Decreased humidity combined with stronger wind greatly enhanced the fire potential, especially over the Cascade Mountains, where fires were the most intense, and the LFP index increased by >100% (Fig. 2F).

With wildfire emissions scaled according to their correlation with LFP, we conducted another simulation by excluding the smoke-induced perturbations in meteorology. As illustrated in Fig. 2G, fire-weather feedback, including both fire emission enhancement and the aerosol-PBL interaction, substantially aggravated the smoke pollution, with a $PM_{2.5}$ increment exceeding 300 μg/m^3 in the Oregon Cascades. Such an aggravation of air pollution substantially increased human smoke exposure, especially in densely populated valley cities. Our estimation shows that fire-weather feedback increased the $PM_{2.5}$ exposure by ~77% in the US West Coast (40 μg/m^3), 48% of which was directly caused by emission enhancement and the other 29% by the aerosol-PBL interaction (fig. S7).

Likewise, monsoon-dominated Southeastern Asia suffers from intense wildfires in spring (*23*), which also features an obvious interannual and synoptic-scale variability (figs. S8 and S9). Comparatively, the fluctuation of wildfires in Southeastern Asia is highly sensitive to rainfall (Fig. 1E) (*20*, *29*). The meteorological evolution during the extreme wildfire events demonstrates that the burned area is inversely correlated with precipitation with a time period of ~2 weeks (Fig. 3B). On a daily basis, the burned area of wildfires in this region shows a good correlation with the fire weather index (FWI) (see the supplementary materials), and the most important contributor to the fire risk is rainfall rate (fig. S10).

Extreme wildfires hit Southeastern Asia in the spring every few years (Fig. 3A). Here, we mainly focused our modeling on the most devastating fire, which engulfed the Indo-China Peninsula in March 2004. On the basis of the validated model simulations (figs. S11 and S12), we found that the prevailing westerlies

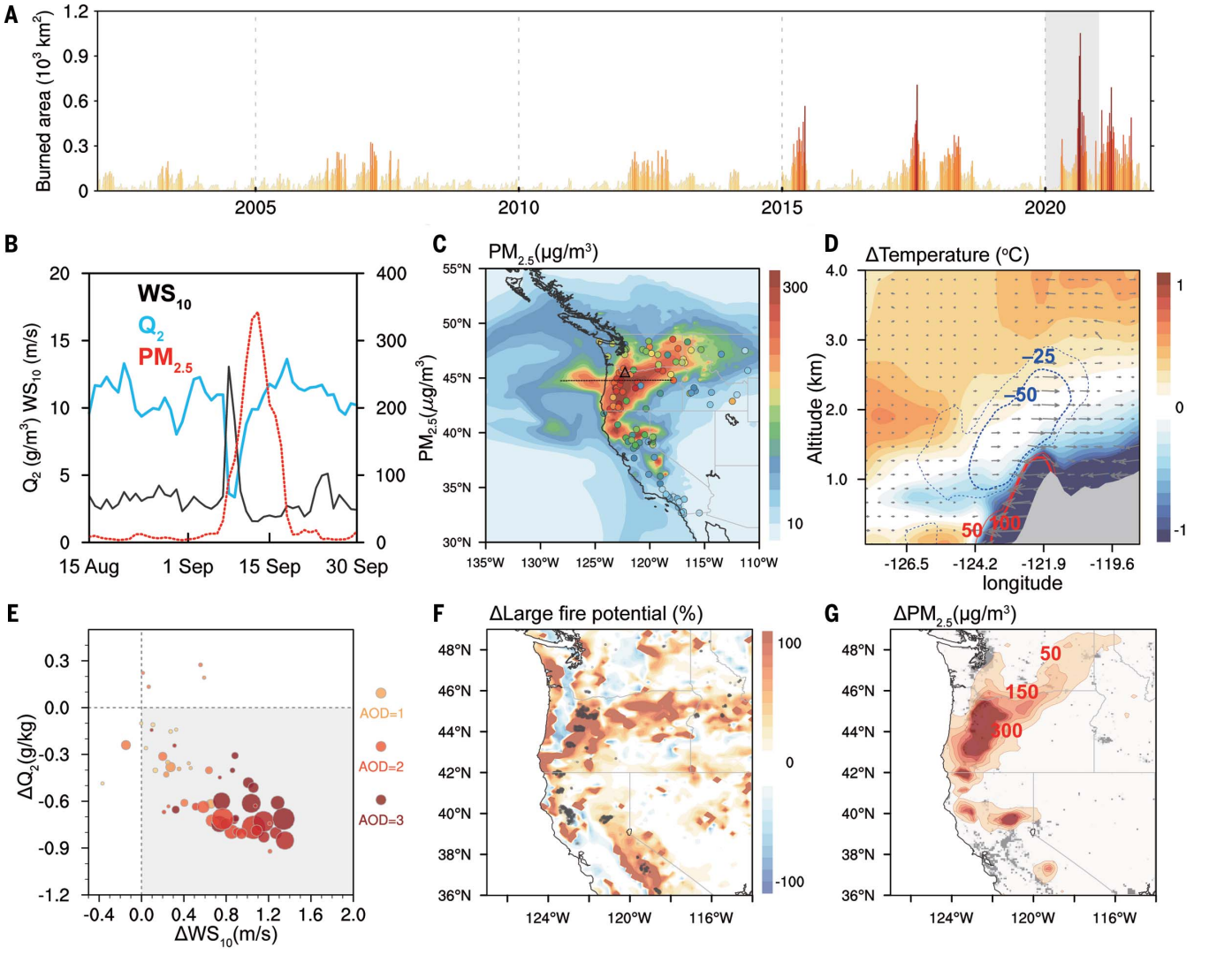

Fig. 2. Fire-weather feedback and aggravated smoke pollution in the US West Coast. (**A**) Time series of satellite-observed daily burned area in the US West Coast (red rectangle in Fig. 1A) in August and September of 2002–2021. (**B**) Daily $PM_{2.5}$, 2-m humidity (Q_2), and WS_{10} observations in the Oregon Cascades in August and September of 2020 [gray shading in (A)]. $PM_{2.5}$ and meteorological observational stations are marked by dots and triangle in (C). (**C**) Simulated (contour) and observed (dots) $PM_{2.5}$ concentrations during 10 to 13 September 2020 in the US West Coast. (**D**) Cross section of ARI-induced temperature, wind, and $PM_{2.5}$ changes (isolines in units of μg/m^3) along the dashed line in (C) based on model simulations. Red and blue isolines show the increase and decrease due to ARI in $PM_{2.5}$ concentrations, respectively. (**E**) Scatter plot of simulated changes in near-surface wind speed and specific humidity due to the radiative effect of aerosol with different AOD levels. (**F**) Changes in LFP caused by the radiative effect of smoke aerosol. Gray dots mark fire spots. (**G**) Population density (gray) and simulated near-surface $PM_{2.5}$ increase (red contour) due to fire-weather feedback.

transported fire-emitted pollutants at an altitude of ~3 km, leading to a thick, BC-containing plume covering almost all of Southeastern Asia (*23*). The light-absorbing fire smoke aloft trapped the radiative energy that would otherwise have warmed the ground surface, causing atmospheric heating and a surface dimming (Fig. 3), which even reached up to +3.0°C and −3.2°C, respectively, averaged over the 2-week burning period (13 to 21 March 2004) (fig. S11C). The opposite temperature responses in the vertical dimension then formed a very stable stratification in the lower troposphere. Meanwhile, the pronounced cooling over the land surface and warming over the sea substantially narrowed the temperature difference between land and sea, forcing a cyclonic circulation anomaly along the coast (Fig. 3E and fig. S13).

The mechanism of the smoke-PBL-cloud-monsoon interaction in this region has been thoroughly discussed (*23*), and our simulations suggest that such feedback could also strongly influence precipitation and promote more intense wildfires in Southeastern Asia. As shown in Fig. 3E, the precipitation was substantially diminished (~7 mm/day), which could be attributed to weakened convection and less moisture transport with anomalous offshore winds. The adjusted circulation blocked the water vapor supply from the South China Sea, thereby leading to a moisture deficit and much less rainfall in the fire-intensive region. Compared with the aerosol-cloud interaction, the radiative effects of smoke aerosol dominated the precipitation suppression (fig. S14). Subsequently, less rainfall was conducive to fire ignition and expansion, further corroborated by the exponential relationship between FWI and burned area (fig. S8). On the

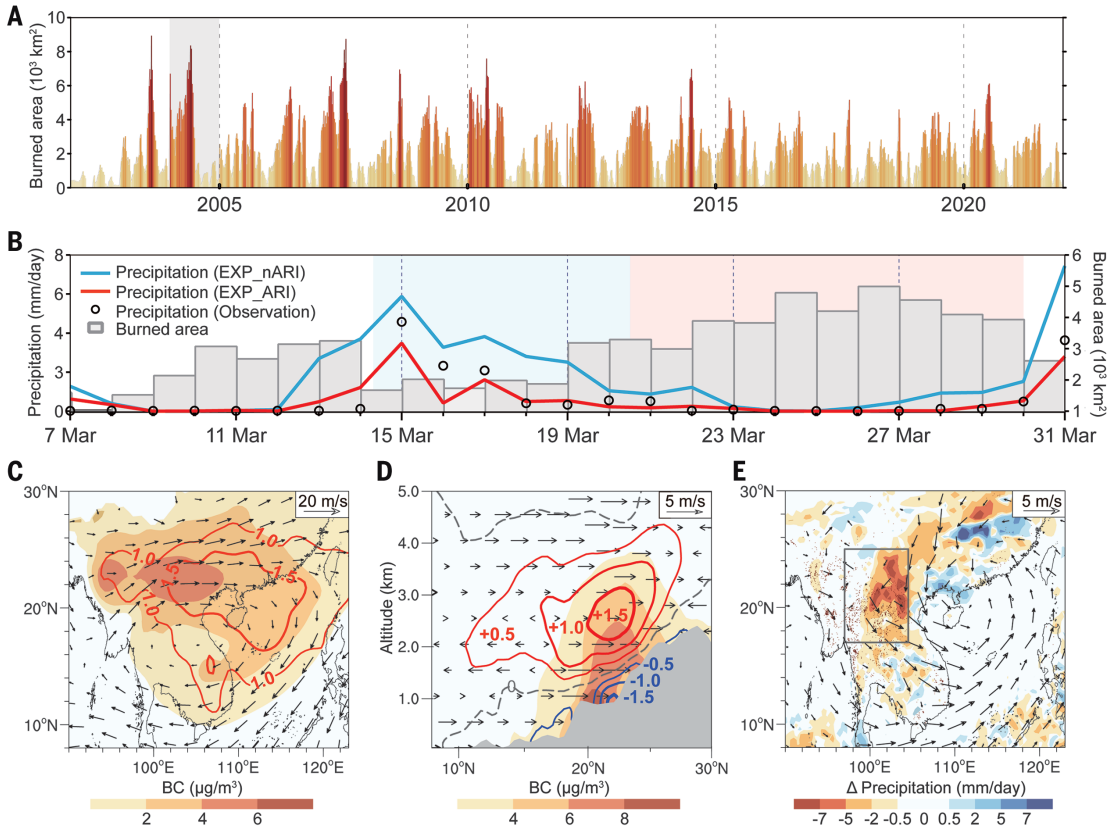

Fig. 3. Fire-weather feedback in Southeastern Asia. (**A**) Time series of satellite-observed daily burned area of Southeastern Asian wildfires (red rectangle in Fig. 1A) in March and April of 2002–2021. (**B**) Daily satellite-detected burned area, precipitation observations from the TRMM multi-satellite product, and corresponding simulations with and without aerosol feedback in March 2004 in the fire-intensive region [black rectangle in (E)]. (**C**) Simulated BC concentration and atmospheric heating (isolines in units of °C) at an altitude of 3 km over Southeastern Asia during the burning period (13 to 21 March 2004). (**D**) Cross section of simulated BC aerosol, air temperature (isolines in units of °C), and wind changes due to the radiative effect of smoke aerosols between longitudes outlined in (E). (**E**) Simulated changes in precipitation and wind due to the radiative effect of aerosols overlaid by 850-hPa wind. Red dots mark the fire spots from satellite observations.

basis of this relationship, we estimated the enhanced smoke pollution resulting from the reduction in precipitation. As shown in fig. S15, $PM_{2.5}$ concentration soared by 300 μg/m^3 in the fire-prone areas. Such a spike in smoke pollution caused by fire-weather feedback would increase $PM_{2.5}$ exposure by ~17% in Southeastern Asia. Similar fire-weather feedback through precipitation suppression also holds true in other years with extreme wildfires (fig. S16).

These results provide a comprehensive demonstration of unexpectedly strong feedback between wildfire and weather in diverse coastal regions. Increasing wildfire severity is not just a consequence of fire-prone weather, it is also an active participant. In a Mediterranean climate with dry and hot summers, such as that in the US West Coast, increased aerosol loading from wildfire suppresses the development of the PBL and enhances orographic winds, thereby increasing the large fire potential at the western slope of the Cascade Mountains through higher wind speed and lower humidity. Conversely, in the fire-intensive region of Southeastern Asia, which has a monsoon climate, thick fire smoke tends to cool the land surface but warm the atmosphere over the sea. The opposite air temperature responses over the land and sea modify the monsoon circulation and block the onshore transport of moisture, thereby suppressing rainfall. More flammable vegetation due to the hydrologic drought intensifies the fire activities and prolongs the burning period. Moreover, in both regions, the aerosol-PBL interaction exacerbates $PM_{2.5}$ concentrations near the surface by suppressing convection and weakening diffusion. The strengthened wildfire emission further enhances the haze pollution and reinforces the positive feedback loops, and thus human exposure to smoke pollution could be greatly amplified (Fig. 4). Although the feedbacks for the two different climatic zones on the east and west coasts appear different, in essence, they can be well explained by a unified mechanism. Both are driven by the radiative effects of fire smoke over different land covers and terrains, which cause thermal contrast and thus enhanced fire emission by modifying circulations and water vapor transport.

Our findings emphasize the complexity of fire-weather feedback in the Earth system and the critical importance of improving our understanding of such mechanisms to prioritize fire prevention and suppression efforts and thus mitigate the impacts of extreme wildfires. The results indicate a potential nonlinear benefit from early fire suppression efforts. Given the persistence and spread of wildfires and fire-weather feedback, early-stage fire suppression at preidentified amplifier regions based on near-real-time forecasting could avert some extreme wildfires. Moreover, strategic and early fire management, e.g., more effort on fire suppression in the forests upslope of populated areas, could reduce the impacts of wildfire-related air pollution and save lives (*30*). As extreme wildfires become increasingly common, coordinated and effective management of fire risks is vital. Meanwhile, growing supercomputing resources and innovative methods

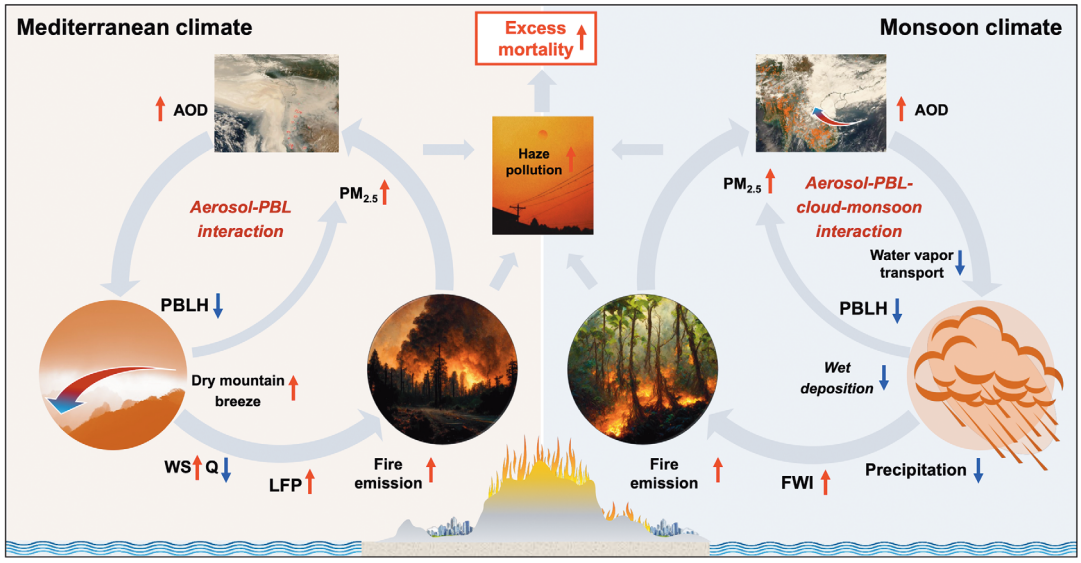

Fig. 4. Conceptual model of the fire-weather feedback in the Mediterranean and monsoon climate regimes. Gray arrows indicate the linkage among wildfire, air quality, and thermal circulations. Red and blue arrows show the increase and decrease, respectively, of each parameter. Q, specific humidity; PBLH, planetary boundary layer height.

are making chemical-weather forecasts ever more feasible. Our results thus suggest that seamless meteorology-chemistry–coupled modeling may be a practical approach for mitigating extreme and damaging fires in populated coastal regions.

REFERENCES AND NOTES

1. M. O. Andreae, *Atmos. Chem. Phys.* **19**, 8523–8546 (2019).
2. D. A. Jaffe *et al.*, *J. Air Waste Manag. Assoc.* **70**, 583–615 (2020).
3. R. Aguilera, T. Corringham, A. Gershunov, T. Benmarhnia, *Nat. Commun.* **12**, 1493 (2021).
4. J. Lelieveld, J. S. Evans, M. Fnais, D. Giannadaki, A. Pozzer, *Nature* **525**, 367–371 (2015).
5. P. G. Curtis, C. M. Slay, N. L. Harris, A. Tyukavina, M. C. Hansen, *Science* **361**, 1108–1111 (2018).
6. W. M. Jolly *et al.*, *Nat. Commun.* **6**, 7537 (2015).
7. M. R. Alizadeh *et al.*, *Proc. Natl. Acad. Sci. U.S.A.* **118**, e2009717118 (2021).
8. N. Andela *et al.*, *Science* **356**, 1356–1362 (2017).
9. A. B. Leverkus, S. Thorn, D. B. Lindenmayer, J. G. Pausas, *Science* **370**, 416–417 (2020).
10. J. T. Abatzoglou, D. E. Rupp, L. W. O'Neill, M. Sadegh, *Geophys. Res. Lett.* **48**, e2021GL092520 (2021).
11. J. L. Crockett, A. L. Westerling, *J. Clim.* **31**, 341–354 (2018).
12. W. C. Bessie, E. A. Johnson, *Ecology* **76**, 747–762 (1995).
13. B. M. Collins, *Agric. For. Meteorol.* **189–190**, 30–35 (2014).
14. M. Goss *et al.*, *Environ. Res. Lett.* **15**, 094016 (2020).
15. D. A. Peterson *et al.*, *Bull. Am. Meteorol. Soc.* **96**, 229–247 (2015).
16. R. D. Field, G. R. Van Der Werf, S. S. P. Shen, *Nat. Geosci.* **2**, 185–188 (2009).
17. N. J. Nauslar, J. T. Abatzoglou, P. T. Marsh, *Fire (Basel)* **1**, 18 (2018).
18. X. Zhou *et al.*, *Sci. Adv.* **7**, eabi8789 (2021).
19. I. C. Yadav *et al.*, *Environ. Pollut.* **227**, 414–427 (2017).
20. M. J. Wooster, G. L. W. Perry, A. Zoumas, *Biogeosciences* **9**, 317–340 (2012).
21. M. G. Pereira, J. Parente, M. Amraoui, A. Oliveira, P. M. Fernandes, in *Extreme Wildfire Events and Disasters: Root Causes and New Management Strategies*, F. Tedim, V. Leone, T. K. McGee, Eds. (Elsevier, 2019); pp. 55–72.
22. T. C. Bond *et al.*, *J. Geophys. Res. Atmos.* **118**, 5380–5552 (2013).
23. K. Ding *et al.*, *Nat. Commun.* **12**, 6416 (2021).
24. A. J. Ding *et al.*, *Atmos. Chem. Phys.* **13**, 10545–10554 (2013).
25. M. S. Khorshidi *et al.*, *Environ. Res. Lett.* **15**, 104002 (2020).
26. C. D. McClure, D. A. Jaffe, *Proc. Natl. Acad. Sci. U.S.A.* **115**, 7901–7906 (2018).
27. A. J. Ding *et al.*, *Geophys. Res. Lett.* **43**, 2873–2879 (2016).
28. T. Rolinski, S. B. Capps, W. Zhuang, *Weather Forecast.* **34**, 257–275 (2019).
29. D. L. A. Gaveau *et al.*, *Sci. Rep.* **4**, 6112 (2014).
30. M. A. Moritz *et al.*, *Nature* **515**, 58–66 (2014).

ACKNOWLEDGMENTS

We are grateful to the High-Performance Computing (HPC) and the Massive Data Center (MDC) of the School of Atmospheric Sciences at Nanjing University, for doing the numerical calculations for this study on its Blade cluster system; the Jiangsu Collaborative Innovation Center for Climate Change for support; and the National Aeronautics and Space Administration (NASA) for the use of imagery from the NASA Worldview application, part of the NASA Earth Observing System Data and Information System (EOSDIS). **Funding:** This work was supported by the National Natural Science Foundation of China (grant 41725020 to A.D., grant 41922038 to X.H., and grant 13001146 to K.D.), by Fundamental Research Funds for the Central Universities (grant 14380187 to X.H.), and by the Tencent Foundation through the XPLORER PRIZE to A.D. **Author contributions:** Conceptualization: X.H., A.D.; Funding acquisition: X.H., A.D.; Investigation: X.H., K.D., J.L., Z.W., L.X.; Methodology: X.H., K.D., J.L., R.T., H.W., Q.Z.; Project administration: X.H., A.D.; Supervision: X.H., A.D.; Visualization: X.H., K.D., J.L.; Writing – original draft: X.H., A.D.; Writing – review and editing: X.H., A.D., Q.Z., S.J.D., Z.-M.T., C.F., M.O.A. **Competing interests:** The authors declare no competing interests. **Data and materials availability:** MODIS thermal anomalies and aerosol products are available at https://ladsweb.modaps.eosdis.nasa.gov/archive/allData/6/MOD14A1/ and https://ladsweb.modaps.eosdis.nasa.gov/archive/allData/61/MOD04_L2/. Fire emissions data are openly accessible at https://www.acom.ucar.edu/Data/fire/. The gridded anthropogenic emission data EDGAR are available from https://edgar.jrc.ec.europa.eu/. Ambient air quality monitoring data can be obtained at https://aqs.epa.gov/aqsweb/airdata/download_files.html. The radiosonde and surface meteorological observations are archived at the National Center for Environmental Information, available at ftp://ftp.ncdc.noaa.gov/pub/data/noaa/ and ftp://ftp.ncdc.noaa.gov/pub/data/igra. The gridded population density data are available at https://sedac.ciesin.columbia.edu/data/collection/gpw-v4. Code used to analyze the data are available from https://github.com/xinhuang415/extremewildfire. The source code of the WRF-Chem model is archived in the UCAR data repository (https://www2.mmm.ucar.edu/wrf/users/download).

SUPPLEMENTARY MATERIALS

science.org/doi/10.1126/science.add9843
Materials and Methods
Figs. S1 to S16
Tables S1 and S2
References (*31*–*37*)

Submitted 17 July 2022; accepted 3 January 2023
10.1126/science.add9843